Nanoscale

PAPER

View Article Online
View Journal | View Issue

Cite this: *Nanoscale*, 2026, **18**, 4104

Probing Mie scattering effects of Si-embedded Ge spherical QD arrays using Raman analysis

Shih-Hsiang Yang,[a] Maria Isabel Alonso,[b] Horng-Chih Lin[a] and Pei-Wen Li *[a]

Received 11th December 2025,
Accepted 7th January 2026

DOI: 10.1039/d5nr05206h

rsc.li/nanoscale

We reported experimental observation of Mie scattering effects of Si embedded Ge quantum dot (QD) arrays. The interaction of Ge QDs with Si nanolayers is characterized by surface enhanced Raman scattering (SERS) of longitudinal optical (LO) Si phonons by the strong electromagnetic fields of Ge QDs. The Mie effect is further evidenced from μ-disk arrays of Si-embedded Ge QDs, in which enhanced optical emission and heightened SERS of optical Ge and LO-Si phonons occur at the disk's edge. Notably, the LO-Si intensity appears to be an effective signature of near-field optical coupling and radiative transfer between neighboring disks.

Introduction

The scalability and dense integration of Si photonic integrated circuits are accelerated by advanced CMOS manufacturing technology.[1] However, the fundamental limit of classical diffraction restricts the minimum achievable spatial resolution of Si nanophotonics, which remains to be addressed for practical applications. Recently, all-dielectric resonant nanophotonics[2–6] has been an extensive and compelling research subject because of the theoretical promise in increasing the spatial overlay of the mode field with optical nanostructures or quantum dot (QD) emitters/absorbers. The Mie resonance of high refractive index Ge/Si nanostructures enhances both electric- and magnetic-fields at spatial scales below the optical wavelength, surpassing the classical diffraction limits and enabling surface enhanced Raman scattering (SERS).[7,8] Therefore, dielectric nanophotonic structures allow the advancement in integration with microcavities for further boosting the quality factor (*Q*-factor) of nanophotonic active devices even at small mode volumes.[5,6]

Intriguing Mie resonance-enhanced light absorption in periodically arranged silicon nanopillar arrays,[9] SiO_2 embedded Si QDs,[10] and Si embedded Ge QDs[11,12] has been reported. Mie-resonance wavelengths are associated with different multipolar electric and magnetic modes that are highly dependent on the size,[4,5,13–16] shape,[4–6,17] pitch,[4,13] surrounding environment,[14,18,19] and shell thickness[13] of the QDs as well as the collective lattice resonances of the finite-sized arrays within nanoresonators.[13,20,21] Whereas a large ensemble of QDs could be created using epitaxy, these self-assembled QDs grow in irregular shapes (hut, pyramid, and dome)[22] with various sizes and generally scatter randomly throughout the space. Size fluctuations and morphological variations in QDs tend to broaden the optical emission/absorption wavelengths and refractive indices due to quantum size effects. Besides, it is difficult to control the interaction of self-assembled QDs with resonant optical modes due to their random spatial distribution. On the other hand, the coupling strength between QDs and Mie resonant modes is limited by their strong radiative losses.[11] Therefore, a high degree of control over the Ge QD size, shape, and spatial location within Si-based nanoresonators in combination with proper engineering in active photonic cavities is crucial to control the far-field radiation of Mie resonant modes and improve emission efficiency.

We have reported light emission from SiO_2 embedded Ge QDs[23,24] and Si/Si_3N_4 embedded Ge spherical QDs[25–27] that were created in a self-assembled, self-organized manner *via* Ostwald ripening and migration of Ge interstitials within growing SiO_2, Si_3N_4 and Si during the thermal oxidation of lithographically-patterned poly-SiGe structures. Details of Ge QD growth and migration mechanisms have been elaborated elsewhere.[27–30] The engineering strengths of our Ge QDs lie in process-controlled, size-tunable QDs at the designated spatial locations in combination with high-temperature thermal stability up to 900 °C, offering flexibility in the waveguide material choices as well as the co-design and integration of photonic devices.[31] In this work, we report experimentally probing Mie interactions of ordered Ge spherical QDs within Si_3N_4/Si nanolayers in terms of SERS of longitudinal optical (LO) phonons in Si enhanced by Ge QDs and evaluated from Raman mapping and linescan characteristics. Mie effects are further showcased by Si/Si_3N_4 embedded Ge QD μ-disk arrays, in

[a]*Institute of Electronics, National Yang Ming Chiao Tung University, Hsinchu, Taiwan. E-mail: pwli@nycu.edu.tw*
[b]*Institute of Materials Science of Barcelona, ICMAB-CSIC, 08193 Bellaterra, Spain*

which optical Ge/LO Si modes and photoluminescence (PL) display the maximum intensity at the disk's edge and even between disks by enhanced near-field optical coupling.

Experimental

The fabrication of Ge spherical QD arrays within Si_3N_4/Si nanolayers started with a SOI substrate that comprises 30 nm-thick Si and 3 μm-thick buried SiO_2 layers. A bi-layer of 20 nm-thick Si_3N_4 and 60 nm-thick poly-$Si_{0.83}Ge_{0.17}$ was sequentially deposited using low-pressure chemical vapor deposition (LPCVD). Poly-$Si_{0.83}Ge_{0.17}$ pillars with widths of 70 nm and 100 nm in pitches of 120 nm and 800 nm were produced using electron beam lithography and C_4F_8/SF_6 plasma etching (Fig. 1(a), (d) and (e)). Following thermal oxidation in an H_2O environment at 900 °C, ordered Ge QDs with diameters of 45 nm and 60 nm were created within Si_3N_4/Si layers (Fig. 1(b), (f) and (g)). The growing SiO_2 generated by thermally oxidizing the Si content of poly-SiGe pillars was removed using CHF_3 plasma. Following LPCVD of 300 nm-thick Si_3N_4, μ-disks with diameters/spacings of 3 μm/350–550 nm were produced using EBL and CHF_3 plasma (Fig. 1(c) and (h)). Two configurations of Ge QD arrays were studied. One is the planar arrays of SiO_2/Si_3N_4 embedded Ge QDs with a QD diameter of 60 nm in a pitch of 800 nm (that is, the samples do not go through the processes of fabricating μ-disks), and another is Si_3N_4 μ-disk arrays containing SiO_2/Si_3N_4 embedded Ge QDs with a QD diameter of 45 nm in a pitch of 120 nm.

To probe local fields within Ge QD/Si-Si_3N_4 nanostructures, Raman images were obtained with a WITec alpha300 R confocal setup, using 532 nm laser excitation at room temperature and a Nikon Fluor (100×/0.9 NA) objective, giving an estimated spot resolution of 0.35 μm. The pixel size for the images was 0.1 × 0.1 μm^2, as given by the scanning movement of a piezo-motor-driven sample stage. The behavior of excitation light interacting with the Ge QD/Si nanolayer system was analyzed using the commercially available 3-D simulation software COMSOL Multiphysics in terms of electric and magnetic field distribution wherein.

Results and discussion

SiO_2/Si_3N_4 embedded Ge QD array on the SOI

Fig. 2(a) shows a plan-view scanning electron microscopy (SEM) micrograph of a 20 μm × 20 μm array comprising N_{total} = 25 × 25 Ge QDs in a pitch of 800 nm. The cross-sectional scanning transmission electron microscopy (STEM) micrograph (Fig. 2(b)) and electron dispersive X-ray spectroscopy (EDX) elemental maps (Fig. 2(c)–(e)) show that on top of the SOI substrate with a 30 nm-thick Si nanolayer, the fabricated Ge QDs have a diameter of 60 nm and are embedded within SiO_2/Si_3N_4 layers. Our previous works have already reported that Ge QDs are formed by the preferential oxidation of the Si content within poly-$Si_{1-x}Ge_x$ lithographically-patterned pillars to SiO_2 with concurrent Ge segregation.[27–30] The thermodynamic explanation for this phenomenon is based on a large difference in the heats of formation of SiO_2 (−911 kJ mol^{-1}) and GeO_2 (−477 kJ mol^{-1}).[32] Following the complete thermal oxidation of poly-$Si_{0.83}Ge_{0.17}$ pillars, the precipitated Ge nanocrystals are able to decompose the proximal solid layers of Si_3N_4 and even migrate through them in the solid state. Concurrent with the migration process, the Ge nanocrystals grow in size by Ostwald ripening, culminating in complete coalescence[28,33] and ultimately resulting in the formation of a spherical Ge QD

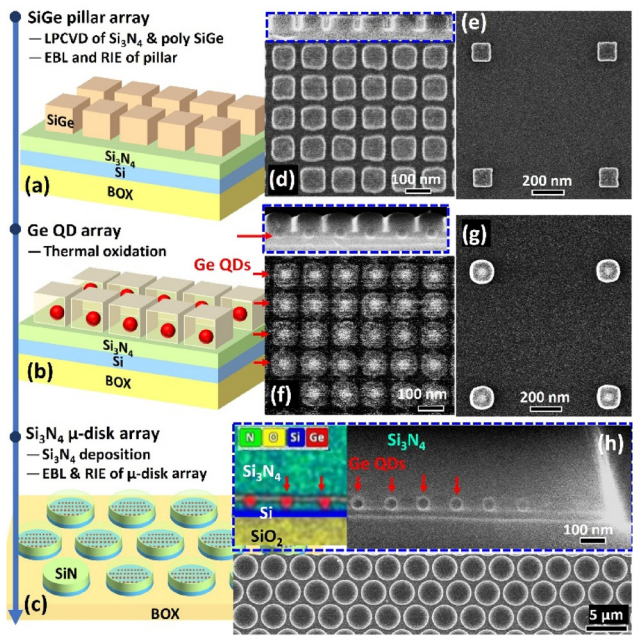

Fig. 1 Process flow, schematic diagrams, and cross-sectional (highlighted by the blue frame) and plan-view scanning electron microscopy (SEM) micrographs for fabricating the Si/Si_3N_4 embedded Ge QD array and the within μ-disk array. Formation of (a) poly-SiGe pillars with widths/pitches of (d) 70 nm/120 nm and (e) 100 nm/800 nm, (b) Ge QDs of (f) 45 nm and (g) 60 nm diameter, and (c)/(h) the Si_3N_4 embedded Si/Ge QD μ-disk array.

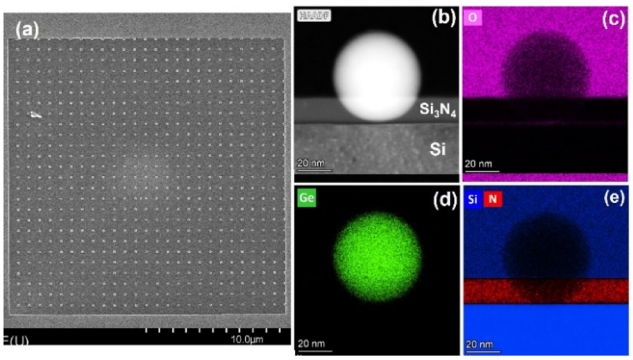

Fig. 2 (a) Plan-view SEM, (b) cross-sectional STEM micrographs, and EDS elemental maps for (c) oxygen, (d) germanium, and (e) silicon of the SiO_2/Si_3N_4 embedded Ge QD array on top of the SOI substrate with a 30 nm-thick Si nanolayer.

per oxidized pillar with both high chemical purity and high degree of crystallinity. Based on the volume conservation, the Ge QD size is essentially determined by the total content of Ge within the poly-$Si_{1-x}Ge_x$ lithographically-patterned pillar and could be controllably tuned by adjusting their width/length/height.[34]

Mie scattering of the SiO_2/Si_3N_4 embedded Ge QD array on the SOI

The Raman spectral characteristics (Fig. 3(a)) measured from the planar SiO_2/Si_3N_4 embedded Ge QD array on top of the SOI substrate show two distinct phonon lines at 308 cm^{-1} and 520 cm^{-1}, corresponding to Ge optical and Si LO phonon modes, respectively. For the studied 60 nm-sized Ge QDs, the Ge optical phonon mode is indeed quite symmetric although broadened with respect to the bulk. The quantum phonon confinement effect induced red-shift in the Ge optical mode is insignificant[35,36] since the studied Ge QD size is larger than the exciton Bohr radius (~24.9 nm) of Ge. Relative to the Ge mode at 301.5 cm^{-1} of bulk Ge, our experimentally observed blue shift of +7.5 cm^{-1} signifies the SiO_2/Si_3N_4/Si-embedded Ge QDs being in a compressive strain of −1.8% on average. No phonon line at 400–410 cm^{-1} is observed, indicating inappreciable Si–Ge mixing in Si/Si_3N_4-embedded Ge QDs. Concurrent with the appearance of an optical Ge phonon line, the intensity of the LO-Si mode originating from the underlying 30 nm-thick Si layer is enhanced compared to that taken at the field out of Ge QDs (the orange-symbol line *versus* the cyan line in Fig. 3(a)). This observation is surprising because the Si Raman signal at the Ge QD positions is expected to be attenuated by a factor close to $-2\alpha d$, where α is the absorption of the Ge QD and d is its diameter.[37]

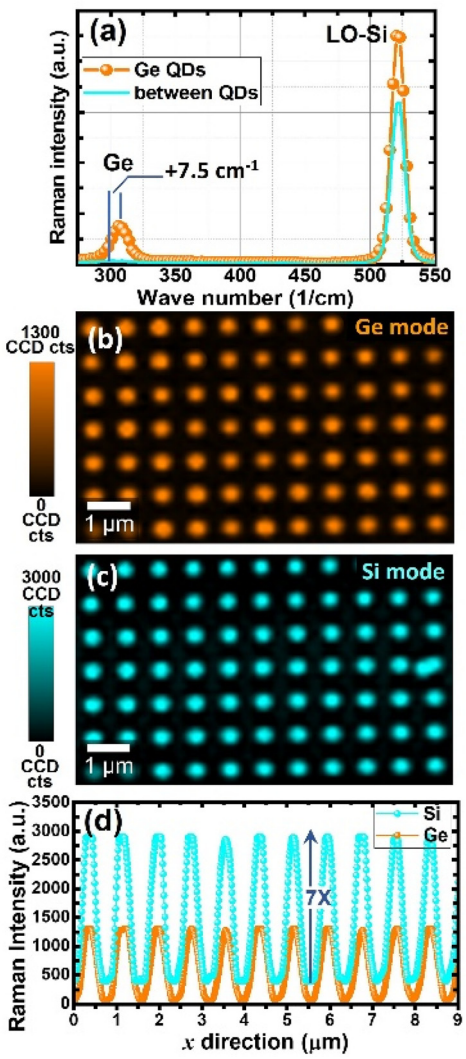

Fig. 3 (a) Raman spectra, plan-view maps of the (b) Ge optical mode and (c) Si LO mode, and (d) linescan profile.

Instead, the interaction of Ge QDs with Si nanolayers is characterized by a large enhancement in Raman scattering of LO-Si phonons by Ge QDs. Raman mapping micrographs show the orthogonal patterns of the Ge optical mode (Fig. 3(b)) and the Si LO mode (Fig. 3(c)) with a pitch of 800 nm, well replicating the spatial arrangement of the Ge QD array (Fig. 2(a)). The Raman linescan profile (Fig. 3(d)) directly points out the fact that the intensity of the LO-Si mode at the spatial locations right below Ge QDs is significantly enhanced 7-fold as compared to that at the field out of QDs, although a uniform 30 nm-thick Si layer is present below the Ge QDs (Fig. 2(b) and (e)). The spatially-periodic enhancement in LO-Si intensity coincides with the locations of Ge QDs, providing direct evidence of Mie effect induced SERS of LO-Si caused by Ge QDs since the Raman intensity scales dramatically with the electric near-field intensity. Similar observations of Raman enhancement in copper phthalocyanine molecules caused by the Mie resonance of the nearby GaP nanoparticles as well as in the copper foil caused by the magnetic dipole resonance of Si nanoparticles have been reported in ref. 38 and 19, respectively.

The refractive index ($n(\lambda)$) of Ge is nearly a constant (n = 4.05) at wavelengths (λ) ranging from 250 nm to 390 nm, reaches the maximum n = 5.86 at λ = 530–540 nm, and then drops to n = 4.2 at λ = 1240 nm−1550 nm.[2] COMSOL simulation (Fig. 4(a)) shows that the excitation light at λ = 532 nm induces a highly concentrated electric field near the surface of the Ge QDs (Fig. 4(b)) and a strong magnetic-field hot-spot inside and near the bottom of the Ge QDs (Fig. 4(c)). Ge QDs directly couple their intense electromagnetic field with the underlying Si layer to cause a large enhancement in the magnetic field locally and solely at the positions underneath the Ge QDs, faithfully and significantly enhancing the Raman signals of the LO-Si mode.

Magnetic resonances in high refractive-index (n) dielectric nanospheres or QDs cause Raman signal enhancement, as was shown by Frizyuk *et al.*[39] in Si nanospheres of 160 nm diameter. In our case, the estimated wavelength of the magnetic dipolar (MD) resonance for a Ge QD with a diameter (d) of 60 nm in air (n_{air} = 1) is ~350 nm according to $\lambda \sim n \times d$ by simply assuming that n_{Ge} is about 5.86 at 532 nm. The MD peak is relatively sharp when the environment is air (n_{air} = 1),

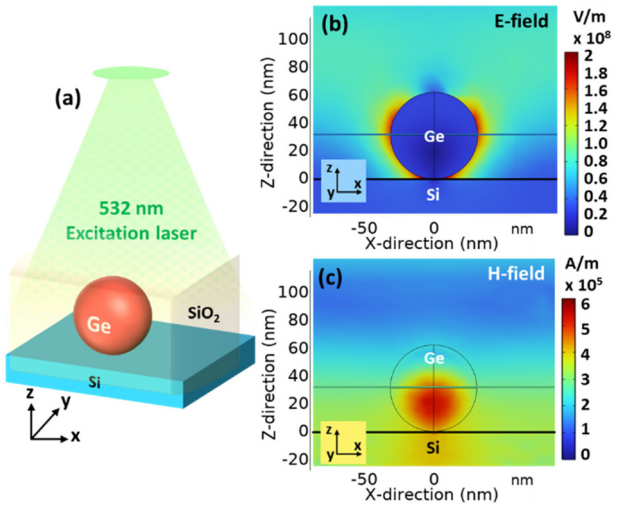

Fig. 4 (a) Schematic diagram of the simulated structure of Ge QD/Si/SiO_2. (b) Electric-field and (c) magnetic-field intensity distributions from the cross-sectional view of the Ge QD/Si system.

whereas for a higher refractive-index surrounding medium, the resonance broadens quickly and extends into the visible range, even if with lower cross section and leaking both into the surrounding and the substrate due to the reduced refractive-index contrast. This leakage favors interaction with the high refractive-index Si substrate, causing an additional enhancement of the scattering cross section, as simulated in ref. 14 for Si nanospheres on top of various dielectric substrates and confirmed with phase change VO_2 as the substrate. Other authors have reported large red shifts of the MD resonance in very small Ge nanodisks[15] and assigned important increases of n_{Ge} up to 8 (for a Ge nanodisk of 100 nm width and height on Si) according to the relationship $\lambda \sim n_{Ge} \times d$. In fact, even if this was interpreted as an effective value for the Ge nanodisks, it is an apparent value of the combined system of the nanosphere on a high refractive-index substrate, as shown in ref. 18. In our case of the planar SiO_2/Si_3N_4 embedded Ge QD array on top of the SOI substrate, we could rule out another possible origin of the measured resonant behavior, such as collective lattice resonances, originating from an interplay between the excitation of MD resonance and diffraction because of the scattering by the periodic arrangement of these spherical QDs, as reported by Evlyukhin *et al.* for Si arrays with suitable lattice periods.[13] For a pitch of 800 nm and an n_{eff} estimated to be ~2.5 for the composed film forming the 2D grating, the Rayleigh–Wood anomaly would be found in the near infrared regime beyond a wavelength of 2 μm. Therefore, we believe that the most plausible explanation for the experimentally observed Raman enhancements in the system of Ge QDs embedded within SiO_2/Si_3N_4 and in contact with Si nanolayers is indeed related to the Mie MD resonance. Further evidence is provided by the performed COMSOL simulation showing local field enhancements considering the relevant spectral range. We believe that these fields are the most likely cause of our experimentally observed enhancement in both Raman modes from the Ge QDs and from the thin Si layer of SOI substrates in contact with the Ge QDs.

Mie resonance of Si embedded Ge QDs within Si_3N_4 μ-disks

Both high *Q*-factors and small mode-volumes are pivotal factors for implementing high-efficiency light emitters. Compared with high *Q*-factors but large mode-volumes from high-order whispering gallery modes (WGMs) in μ-disks, low-order Mie resonances are characterized by smaller mode-volumes but smaller *Q* factors with a wider spectral response. A combined configuration of embedding optical Ge QDs and Si nanoresonators within Si_3N_4 μ-disks appears to provide an effective way to achieve high *Q*-factors and small mode-volumes simultaneously when QD emission matches resonant modes.

Our previous papers[28,31] have already reported the size dependence of Si_3N_4 μ-disks on the cavity modes. Compared to 7 μm and 5 μm μ-disks, 3 μm Si_3N_4 μ-disks indeed significantly reduce the Fabry–Pérot mode number due to their smaller sizes/mode volumes but have considerable radiative loss *via* evanescent fields spreading to regions outside the disks. The light confinement within 3 μm Si_3N_4 μ-disks could be improved by the configuration of the μ-disk array. In this work, further support for Ge QD mediated Si SERS is provided by the Si_3N_4 embedded Si/Ge QD μ-disk array (Fig. 5(a and b)), which is in a hexagonal close packed arrangement with a disk diameter of 3 μm and inter-disk spacings ranging from 350 nm to 550 nm (Fig. 5(c)–(e)). Within the Si_3N_4 μ-disks, the Ge QDs have a diameter of 45 nm and are closely spaced in a pitch of 120 nm (Fig. 5(f)).

Mapping micrographs show that Raman optical Ge (Fig. 6(a))/LO-Si modes (Fig. 6(b)) and PL (Fig. 6(c)) display the

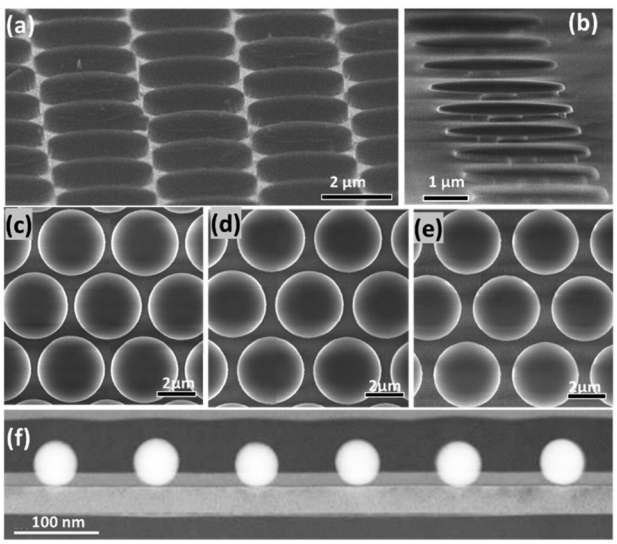

Fig. 5 Si_3N_4 embedded Si/Ge QD μ-disks in a hexagonal close packed arrangement. Tilted SEM micrographs of (a) as fabricated and (b) buried oxide and Si_3N_4 partially removed for clearly showing μ-disks. Plan-view SEM micrographs of μ-disks with inter-disk spacings of (c) 350 nm, (d) 450 nm, and (d) 550 nm. (f) Cross-sectional TEM micrograph of 45 nm Ge QDs in a pitch of 120 nm.

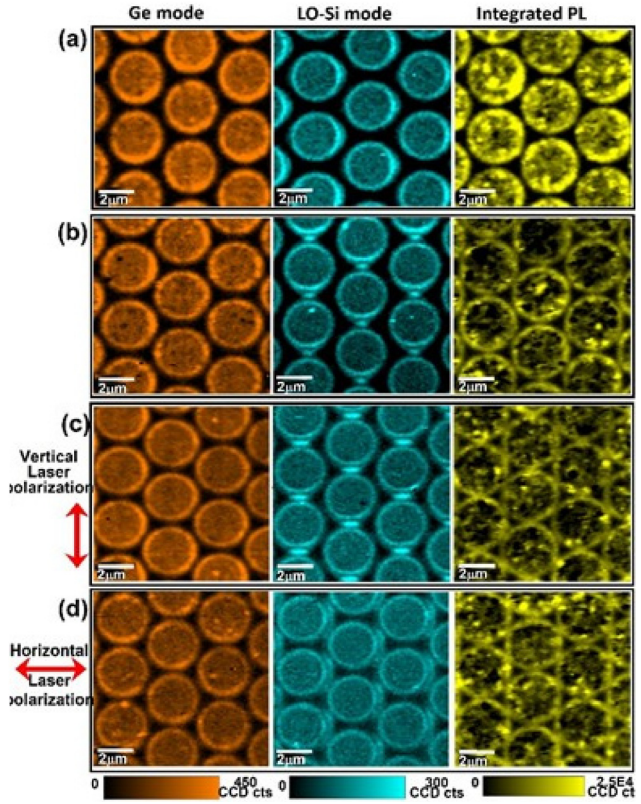

Fig. 6 Mapping micrographs of the Raman Ge optical mode, Si LO mode, and integrated PL of the Ge-QD μ-disk (3 μm in diameter) array with interdisk spacings of (a) 550 nm, (b) 450 nm, and (c) 350 nm with incident vertical laser polarization and (d) 350 nm with incident horizontal laser polarization.

maximum intensity at the disk's edge, which is analogous to the WGM patterns. An interesting finding of note is that on decreasing the inter-disk spacing from 550 nm to 350 nm, the PL circular-ring patterns deform into hexagons accompanied by the emergence of additional LO-Si spots between disks, whereas the circular-ring pattern of the optical Ge mode remains intact. The second interesting finding of note is that the LO-Si intensity appears to be an effective signature of near-field optical coupling and radiative transfer between neighboring disks. It is clearly seen in Fig. 6(b) and (c) that both the intensity and size of the additional LO-Si spots between disks considerably increase when Si-embedded Ge QD μ-disks get closer to each other as a result of a significant enhancement in the electromagnetic near-field intensity. The third interesting finding of note is that the incident laser polarization influences the spatial location of LO-Si inter-disk bright spots but has no obvious effects on the optical Ge mode and PL signals (Fig. 6(c) *versus* Fig. 6(d)). This is possibly ascribed to the higher symmetry and polarization of the Raman mode of the 30 nm-thick c-Si layer in contrast to the rather unpolarized PL and Ge QD Raman signals.

In contrast to the planar SiO_2/Si_3N_4 embedded Ge QD array discussed in the previous section, the Si/Ge QDs embedded in the Si_3N_4 μ-disk resonators are arranged in a square array of a much smaller pitch (~120 nm). The Ge QDs have a smaller diameter of 45 nm which probably does not introduce a qualitative difference compared to the previous case. Even if the isolated QDs in air would have a blue-shifted MD resonance, they would likely have a larger increase of apparent n_{Ge} when placed on the substrate.[14] Hence, the main difference comes from the small pitch. In this case, the composed film forming the 2D grating would also have a larger effective refractive index for diffraction (we estimate it to be n_{eff} ~4) due to a higher density of Ge QDs. Therefore, the Rayleigh–Wood anomaly would be in the visible range, λ ~480 nm, with lattice-mediated collective lattice resonances coming into play as shown in Fig. 7. COMSOL simulation shows that the excitation light at λ = 532 nm induces a highly-concentrated magnetic field within Ge QDs and the intensity significantly increases in magnitude when the QD array of $N_{total} = N \times N$ increases from N = 1 through 20, 40 to infinite, consistent with an increase in quality factor of the lattice mode.

Fig. 8(a) compares PL spectra acquired from the Si_3N_4 μ-disk array containing Ge QDs and not. Si_3N_4 μ-disks containing Si-embedded Ge QDs show sharp Raman-mode peaks at 540 nm (Ge-mode) and 547 nm/560 nm (1st/2nd order Si-modes) in combination with broad and strong PL with major sub-peaks at 585 nm and 620 nm. For comparison, weak PL at λ = 650 nm–750 nm is measured from the reference structure of Si/Si_3N_4 μ-disks, where WGM modes also cause a noticeable but lower resonance effect. Weak photoluminescence of thermal SiO_2/Si structures at 650 nm (ref. 40) and single-photon emission of the Si_3N_4/SiO_2 system at 570 nm–670 nm (ref. 41) at room temperature have also been reported, due to the formation of optically active defects or centers at the SiO_2/Si and Si_3N_4/SiO_2 interfaces. Our experimental observation of strong PL at 585–620 nm from Ge QD Si_3N_4 μ-disks suggests possible PL enhancement of optically active centers due to the Mie scattering effect of the Si-embedded Ge QD system. It is clearly seen in the mapping micrographs of PL and the Si LO-mode that in contrast to faint ring patterns in the Si_3N_4 μ-disks containing no QDs (Fig. 8(c)), distinct regions around the patterns of the Si LO-mode (spots) and PL (hexagons) with much higher CCD counts appear in the Ge-QD μ-disks (Fig. 8(b)).

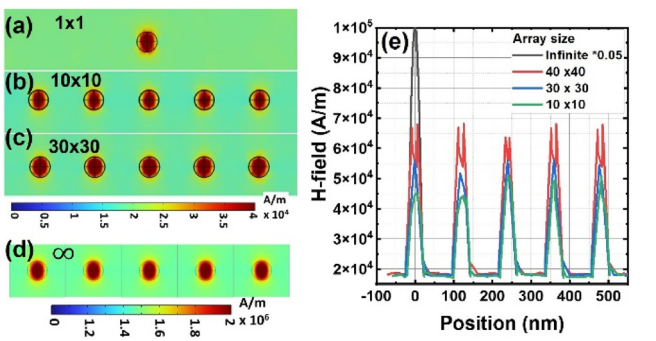

Fig. 7 Magnetic-field intensity distribution from the central portion of the Ge QD/Si array with N_{total} = (a) 1 × 1, (b) 10 × 10, (c) 30 × 30, and (d) infinite. (e) Line scan of the Ge QD array for various sizes of Ge QDs.

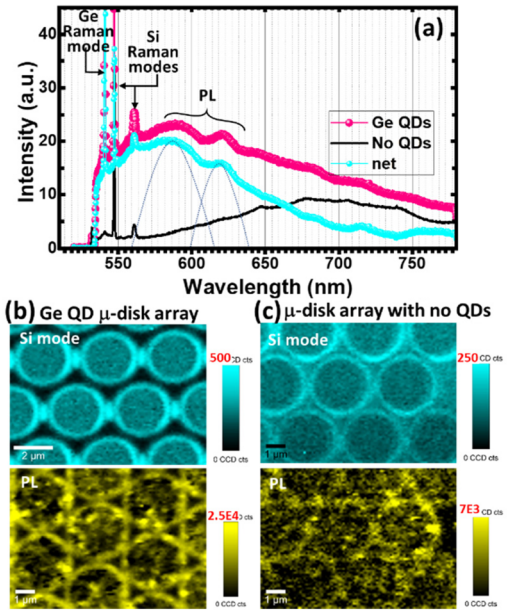

Fig. 8 (a) PL spectra and mapping micrographs of Si LO mode/integrated PL of 3 μm Si_3N_4 μ-disks (b) with and (c) without Ge QDs.

Conclusion

We reported experimental observation of Mie resonance interactions between Ge QDs and Si nanolayers in Si-embedded Ge QD arrays, using Raman spectral and mapping analysis. Mie resonance induced SERS of Si is characterized by a large enhancement in the LO-Si Raman signals solely at the positions underneath the Ge QDs. In μ-disks, a combination of WGMs and Mie resonance is further evidenced by the ring-like patterns of the Ge optical-mode, Si LO-mode, and PL (*i.e.*, the maximum intensity occurs at the disk's edge) in the Si-embedded Ge QD μ-disk arrays. Interestingly, the spectral PL behavior and all measured enhancements are higher in the structures with Ge QDs. Besides, the appearance of additional strong LO-Si Raman signals between μ-disks is an effective signature of strong near-field optical coupling. The nanoscale Mie resonance offers promising potential in implementing nanoemitters and photodetectors. Ultrathin solar cells and self-powered photodetectors have been reported by integrating SiGe-based Mie resonators and Ge QDs or Si nanodisks.[42,43] The experimental feasibility of our Ge QDs in photodetection has also been demonstrated in terms of low dark current in combination with high photoresponsivity and high bandwidths for visible to near-infrared photodetection.[44]

Author contributions

Y. S. H. conducted the fabrication and COMSOL simulation of Ge-QD arrays and μ-disks. M. I. A. conducted μ-Raman measurement, data analysis and manuscript preparation. L. H. C. contributed to data analysis. L. P. W. conceived the study, supervised the work, and contributed to data analysis and manuscript preparation. All authors read and approved the final manuscript.

Conflicts of interest

There are no conflicts to declare.

Data availability

The datasets used and analyzed during the current study are available from the corresponding author on reasonable request.

Acknowledgements

This work was financially supported by the Honghai Research Institute 114UA90042, MA-tek 2025-T-018, and National Science and Technology Council, Taiwan 114-2119-M-A49-005, 113-2927-I-A49-503 and 112-2221-E-A49-162-MY3. M. I. A. acknowledges projects CEX2023-001263-S and PID2022-141956NB-I00 of AEI (Spain), as well as the CSIC (Spain)–NSTC (Taiwan) collaboration BILTW22002. We thank the reviewers very much for the valuable and important comments helping us improve the discussion.

References

1 Y. Su, Y. He, X. Guo, W. Xie, X. Ji, H. Wang, X. Cai, L. Tong and S. Yu, *ACS Photonics*, 2023, **10**, 2020–2030.
2 D. G. Baranov, D. A. Zuev, S. I. Lepeshov, O. V. Kotov, A. E. Krasnok, A. B. Evlyukhin and B. N. Chichkov, *Optica*, 2017, **4**, 814–825.
3 I. Staude, T. Pertsch and Y. S. Kivshar, *ACS Photonics*, 2019, **6**, 802–814.
4 V. E. Babicheva and A. B. Evlyukhin, *Adv. Opt. Photonics*, 2024, **16**, 539–658.
5 M. Hasan and O. G. Hellesø, *Nanotechnology*, 2021, **32**, 202001.
6 K. Koshelev and Y. Kivshar, *ACS Photonics*, 2020, **8**, 102–112.
7 S. Raza and A. Kristensen, *Nanophotonics*, 2021, **10**, 1197–1209.
8 P. A. Dmitriev, D. G. Baranov, V. A. Milichko, S. V. Makarov, I. S. Mukhin, A. K. Samusev, A. E. Krasnok, P. A. Belov and Y. S. Kivshar, *Nanoscale*, 2016, **8**, 9721–9726.
9 F. J. Bezares, J. P. Long, O. J. Glembocki, J. Guo, R. W. Rendell, R. Kasica, L. Shirey, J. C. Owrutsky and J. D. Caldwell, *Opt. Express*, 2013, **21**, 27587–27601.
10 A. Capretti, A. Lesage and T. Gregorkiewicz, *ACS Photonics*, 2017, **4**, 2187–2196.
11 V. Rutckaia, F. Heyroth, A. Novikov, M. Shaleev, M. Petrov and J. Schilling, *Nano Lett.*, 2017, **17**, 6886–6892.

12 V. Rutckaia, F. Heyroth, G. Schmidt, A. Novikov, M. Shaleev, R. S. Savelev, J. Schilling and M. Petrov, *ACS Photonics*, 2020, **8**, 209–217.
13 A. B. Evlyukhin, C. Reinhardt, A. Seidel, B. S. Luk'yanchuk and B. N. Chichkov, *Phys. Rev. B: Condens. Matter Mater. Phys.*, 2010, **82**, 045404.
14 Y. Huang, J. Yan, C. Ma and G. Yang, *Nanoscale Horiz.*, 2019, **4**, 148–157.
15 D. E. Utkin, K. V. Anikin, S. L. Veber and A. A. Shklyaev, *Opt. Mater.*, 2020, **109**, 110466.
16 S. Ishii, K. Chen, H. Okuyama and T. Nagao, *Adv. Opt. Mater.*, 2017, **5**, 1600902.
17 A. B. Evlyukhin, C. Reinhardt and B. N. Chichkov, *Phys. Rev. B: Condens. Matter Mater. Phys.*, 2011, **84**, 235429.
18 N. A. Butakov and J. A. Schuller, *Sci. Rep.*, 2016, **6**, 38487.
19 Y. C. Tseng, T. Y. Lin, Y. C. Lee, C. K. Ku, C. W. Chen and H. L. Chen, *Chem. Mater.*, 2018, **30**, 1472–1483.
20 V. I. Zakomirnyi, A. E. Ershov, V. S. Gerasimov, S. V. Karpov, H. Ågren and I. L. Rasskazov, *Opt. Lett.*, 2019, **44**, 5743–5746.
21 A. D. Utyushev, V. I. Zakomirnyi, V. S. Gerasimov, S. V. Karpov, A. E. Ershov and I. L. Rasskazov, *Photonics*, 2020, **7**, 24.
22 M. I. Alonso, M. de la Calle, J. O. Ossó, M. Garriga and A. R. Goñi, *J. Appl. Phys.*, 2005, **98**, 033530.
23 P. W. Li, M. T. Kuo, W. M. Liao and M. J. Tsai, *Jpn. J. Appl. Phys.*, 2004, **43**, 7788–7792.
24 M. H. Kuo, S. K. Chou, Y. W. Pan, S. D. Lin, T. George and P. W. Li, *J. Appl. Phys.*, 2016, **120**, 233106.
25 Y. H. Kuo, S. H. Chiu, C. W. Tien, S. D. Lin, W. H. Chang, H. C. Lin and P. W. Li, *Nano Futures*, 2020, **4**, 015001.
26 C. Y. Chien, Y. J. Chang, C. C. Wang, M. H. Kuo, W. T. Lai and P. W. Li, *Nanoscale*, 2014, **6**, 5303–5308.
27 I. H. Wang, P. Y. Hong, K. P. Peng, H. C. Lin, T. George and P. W. Li, *IEDM Tech. Dig*, San Francisco, USA, 2020.
28 P. Y. Hong, C. H. Lin, I. H. Wang, Y. J. Chiu, B. J. Lee, J. C. Kao, C. H. Huang, H. C. Lin, T. George and P. W. Li, *Appl. Phys. A*, 2023, **129**, 126.
29 K. H. Chen, C. C. Wang, T. George and P. W. Li, *Appl. Phys. Lett.*, 2014, **105**, 122102.
30 T. George, P. W. Li, K. H. Chen, K. P. Peng and W. T. Lai, *J. Phys. D: Appl. Phys.*, 2017, **50**, 105101.
31 C. H. Lin, P. Y. Hong, B. J. Lee, H. C. Lin, T. George and P. W. Li, *IEEE Trans. Electron Devices*, 2023, **70**, 2113–2120.
32 M. W. Chase, C. A. Daives, J. R. Downey, D. J. Frurip, R. A. McDonald and A. N. Syverud, *JANAF Thermochemical Tables*, American Inst. of Physics, 3rd edn, 1985.
33 C. Y. Chien, Y. J. Chang, K. H. Chen, W. T. Lai, T. George, A. Scherer and P. W. Li, *Nanotechnology*, 2011, **22**, 435602.
34 M. H. Kuo, C. C. Wang, W. T. Lai, T. George and P. W. Li, *Appl. Phys. Lett.*, 2012, **101**, 223107.
35 P. H. Liao, T. C. Hsu, K. H. Chen, T. H. Cheng, T. M. Hsu, C. C. Wang, T. George and P. W. Li, *Appl. Phys. Lett.*, 2014, **105**, 172106.
36 S. Singh, D. K. Rath, S. Kumar, N. Ahlawat, S. Sharma, A. Singh, S. C. Pandey, P. S. Rout, L. Bansal, B. Sahu, S. Srivastava, S. K. Chondath, M. K. Chattopadhyay and R. Kumar, *J. Phys. Chem. C*, 2025, **129**, 13329–13336.
37 M. I. Alonso, E. Bailo, M. Garriga, A. Molero, P. O. Vaccaro, A. R. Goñi, A. Ruiz and M. Alonso, *J. Phys. Chem. C*, 2015, **119**, 22154–22163.
38 S. Hayashi, R. Koh, Y. Ichiyama and K. Yamamoto, *Phys. Rev. Lett.*, 1988, **60**, 1085–1088.
39 K. Frizyuk, M. Hasan, A. Krasnok, A. Alú and M. Petrov, *Phys. Rev. B*, 2018, **97**, 085414.
40 A. P. Baraban, S. N. Samarin, V. A. Prokofiev, V. A. Damitriev, A. A. Selivanov and Y. Petrov, *J. Lumin.*, 2019, **205**, 102–108.
41 A. Senichev, Z. Martin, S. Peana, D. Sychev, X. Xu, A. Lagutchev, A. Boltasseva and V. M. Shalaev, *Sci. Adv.*, 2021, **7**, eabj0627.
42 M. Aouassa, M. Bouabdellaoui, W. B. Pessoa, I. Berbezier, T. Kallel, T. Ettaghzouti, M. Yahyaoui, K. M. Saron, A. K. Aladim, M. Ibrahim and I. Althobaiti, *ACS Appl. Electron. Mater.*, 2024, **6**, 3290–3296.
43 M. Aouassa, M. Bouabdellaoui, W. B. Pessoa, A. Tsarev, M. Ibrahim, A. K. Aladim, K. M. A. Saron and I. Berbezier, *J. Mater. Sci.: Mater. Electron.*, 2025, **36**, 394.
44 M. H. Kuo, M. C. Lee, H. C. Lin, T. George and P. W. Li, *Sci. Rep.*, 2017, **7**, 44402.